





RESEARCH ARTICLE | AUGUST 19 2024

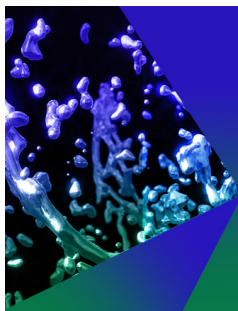
Azimuthal ion dynamics at the inner pole of an axisymmetric Hall thruster

Parker J. Roberts   ; Vernon H. Chaplin  ; Benjamin A. Jorns 



Phys. Plasmas 31, 083513 (2024)

<https://doi.org/10.1063/5.0214477>



Azimuthal ion dynamics at the inner pole of an axisymmetric Hall thruster

Cite as: Phys. Plasmas **31**, 083513 (2024); doi: [10.1063/5.0214477](https://doi.org/10.1063/5.0214477)

Submitted: 17 April 2024 · Accepted: 27 July 2024 ·

Published Online: 19 August 2024



View Online



Export Citation



CrossMark

Parker J. Roberts,^{1,a)}  Vernon H. Chaplin,²  and Benjamin A. Jorns¹ 

AFFILIATIONS

¹Department of Aerospace Engineering, University of Michigan, Ann Arbor, Michigan 48105, USA

²Jet Propulsion Laboratory, California Institute of Technology, Pasadena, California 91109, USA

^{a)} Author to whom correspondence should be addressed: pjrob@umich.edu

ABSTRACT

The azimuthal dynamics of ions along the inner pole of a Hall thruster with a centrally mounted cathode and a magnetic shielding topography are experimentally investigated. A time-averaged laser-induced fluorescence diagnostic is implemented to characterize the azimuthal ion velocity distribution, and its moments are computed numerically to infer bulk rotation speed and ion temperature. It is found that the time-averaged ion swirl velocity grows to 2 km/s in the near-pole region, and the cathode ions exhibit ion temperatures in the azimuthal direction approaching 8 eV. Both of these quantities exceed the speeds and temperatures anticipated from classical acceleration and heating. Time-resolved laser-induced fluorescence is then employed to investigate the role of plasma fluctuations in driving the time-averaged ion properties. Semicohherent fluctuations at 90 kHz are observed in the ion velocity distribution and its associated moments. These oscillations are correlated with the gradient-driven anti-drift wave, which propagates azimuthally in the near-field cathode plume. Quasilinear theory is used to construct a 1D model for acceleration and heating of the ion population as a result of the anti-drift mode. This approach demonstrates qualitative agreement with the time-averaged ion velocity and temperature, suggesting that the anti-drift mode may be a dominant driver of azimuthal ion acceleration and heating in front of the cathode keeper and the inner half of the inner front pole cover. These results are discussed in terms of their relevance to the erosion of thruster surfaces in the near-field cathode plume.

© 2024 Author(s). All article content, except where otherwise noted, is licensed under a Creative Commons Attribution (CC BY) license (<https://creativecommons.org/licenses/by/4.0/>). <https://doi.org/10.1063/5.0214477>

I. INTRODUCTION

Understanding the lifetime-limiting mechanisms of the Hall effect thruster is critical for enabling next-generation deep space missions. This device is a form of in-space electric propulsion, which leverages an $E \times B$ discharge to accelerate ions through a quasineutral plasma.¹ Hall thrusters are attractive compared to other forms of electric propulsion due to their ability to achieve high thrust density while maintaining high specific impulse (>2000 s).² While these features have led to the widespread use of this technology for Earth-orbiting satellites,³ challenges with thruster lifetime have historically limited their applicability for deep space missions.

Recent Hall thruster designs have incorporated a technology known as magnetic shielding, which prolongs device lifetime by eliminating traditional erosion mechanisms at the thruster discharge channel walls.^{4,5} This is accomplished by a precisely curved magnetic field shape in the thruster channel, which results in electric fields at the channel walls that repel ions. Wear tests have shown that by ameliorating this erosion process, thruster lifetimes can be increased by more

than a factor of 1000,^{6–8} enabling the use of Hall thrusters for longer-duration missions exceeding 10 000 h.⁹ These experiments also revealed previously unnoticed erosion at the magnetic poles of the device.^{10,11} While this pole erosion is more gradual than the rate of channel erosion in thrusters without magnetic shielding, it may still pose a lifetime risk for extended operational lifetimes. It is therefore crucial to quantify and mitigate lifetime risks due to pole erosion in Hall thrusters. A major challenge, however, is that the processes responsible for this erosion are not fully understood.

Because of this lifetime risk, extensive research has explored the mechanisms responsible for the observed rates of ion sputtering at the poles. The multi-fluid/hybrid-PIC code Hall2De¹² was used to demonstrate that in some cases, pole sputtering rates could be accounted for via so-called “classical” effects,^{10,13,14} namely, as a result of divergent ions induced by the downstream potential shift, which accompanies magnetically shielded topographies.¹⁵ However, in certain thrusters and operating conditions, these classical effects alone have led to underpredictions of erosion rates measured in wear tests.¹⁶ Motivated

by this discrepancy, laser-induced fluorescence (LIF) experiments were performed to directly measure the ion properties in the vicinity of the pole.^{13,17,18} These studies found that the near-pole ion temperature exceeded model predictions, leading to the hypothesis that plasma turbulence due to microscopic instabilities could heat the ions and explain the observed erosion rates.¹⁸

In particular, an emphasis has been placed on effects related to the lower-hybrid drift instability (LHDI) and the modified two-stream instability (MTSI), due to the fact that these waves are not subject to strong ion Landau damping in the pole plasma environment and can therefore lead to ion heating.^{19–22} Indeed, simplified models for ion heating based on predicted LHDI growth rates show an improvement in erosion rate predictions.¹⁸ However, there is as of yet no direct evidence for the presence of these instabilities in the Hall thruster plume.

While the existence of LHDI is a promising candidate to explain erosion, it is also possible that lower-frequency oscillations contribute. It has been shown experimentally that the near-field plasma in the cathode of Hall thrusters can support a gradient-driven rotational wave with relatively low frequency (<100 kHz) and large amplitude (50% of mean plasma properties peak-to-peak).^{23,24} Given the larger fluctuations in plasma potential associated with these modes, it is possible that they may transfer azimuthal energy to cathode-born ions as they propagate and increase pole sputtering rates. Correlationally, this would be consistent with wear measurements demonstrating azimuthal shadowing of the erosion profile of the cathode keeper surface, which suggests large azimuthal ion swirl.²⁵ Due to the potentially large effect that these intense fluctuations in the azimuthal electric field may have on the ion population originating at the cathode and traversing the pole, there is a need to investigate the link between these waves and the near-pole ion dynamics.

We address this need by measuring azimuthal velocities of singly charged xenon ions in a Hall thruster cathode plume with time-resolved laser-induced fluorescence velocimetry. This paper is organized in the following way. In Sec. II, we summarize the theory of the gradient-driven mode in the cathode plasma environment and outline the nonlinear mechanism by which this wave may energize ions near the thruster pole. Following this, we construct a 1D model of the wave-particle interaction, which relates time-averaged ion properties to the amplitude of the mode. In Sec. III, we describe our experiment to characterize the time-resolved behavior of the ion distribution in the azimuthal direction, while in Sec. IV, we describe our methods for extracting both time-averaged and time-resolved ion properties from these measurements. Section V then includes a comparison between the results of these experiments and the predictions of our ion acceleration model, while in Sec. VI, we discuss these results in the context of other research to understand the source of energetic ions near the Hall thruster pole. Finally, we summarize the key conclusions in Sec. VII.

II. THEORY

In this section, we first describe the linear two-fluid theory for the dispersion of the azimuthally propagating anti-drift wave in the plume of a centrally mounted Hall thruster cathode. We then apply a quasilinear argument to demonstrate the nonlinear mechanism of wave-induced force and energy transfer to the ions from the gradient-driven electron drift. Finally, we develop a simplified 1D model for the impact of these wave effects on ions expanding radially from the cathode plume, in order to foster comparison with laser-induced fluorescence data.

A. Properties of anti-drift waves

Figure 1 shows a photograph of a Hall effect thruster operating with a centrally mounted cathode. This device is characterized by an annular channel with a radial magnetic field, across which an axial electric field accelerates ions. The hollow cathode, in this case located on the axis of symmetry, sources electron current which both neutralizes the plume ions and completes the circuit to the anode. A by-product of producing a large radial magnetic field is that near the device axis, the magnetic field vector is close to axial. Discharge current from the cathode primarily flows parallel to this locally axial magnetic field, while steep gradients in plasma density and electric potential form in the radial direction.²⁴ These radial gradients in the cathode region drive a relative drift between ions and electrons in the azimuthal direction, which in turn can serve as an energy source for plasma instabilities.

The key instability of interest in this work is the so-called anti-drift wave, which is a rotational, low-frequency oscillation (<100 kHz).^{23,24} Following Ref. 24, the dispersion relation, $\omega(\vec{k})$, for this mode is derived from a two-fluid model in local Cartesian coordinates:

$$\frac{k^2 c_s^2}{(\omega - \vec{k} \cdot \vec{u})^2} = \frac{i\nu_{pl} - k_y u_D}{\omega + k_y u_{E \times B} - k_z u_{eoz} - k_y u_D + i\nu_{pl}}. \quad (1)$$

Here, ω is the angular frequency of the mode, and $\vec{k} = k_y \hat{y} + k_z \hat{z}$ is the wavevector, which is represented in a local Cartesian coordinate system defined by $\hat{y} \rightarrow \hat{\theta}$ and $\hat{x} \rightarrow \hat{r}$. We also have introduced c_s , the ion sound speed; u_D , the electron diamagnetic drift; $u_{E \times B}$, the electron $E \times B$ drift speed; u_{eoz} , the axial electron drift, and \vec{u} , the axial ion drift velocity. We omit subscripts on quantities related to the ion fluid in this work. The parameter $\nu_{pl} = k_z^2 k_B T_e / (m_e \nu_e)$ quantifies the effect of electron-neutral collisions and depends on the electron temperature T_e , the electron mass m_e , and the electron-neutral collision frequency ν_e . Physically, the anti-drift wave described by Eq. (1) is characterized by a low-frequency, quasineutral ion response to electric field and density fluctuations, which propagate at the electron diamagnetic drift speed. These waves travel primarily in the azimuthal direction due to the strong electron drift; however, they grow unstable as a result of a small but finite axial component of the wavevector. Specifically, electron-neutral collisions along magnetic field lines cause a phase delay between fluctuations in plasma potential, ϕ_1 , and plasma density,

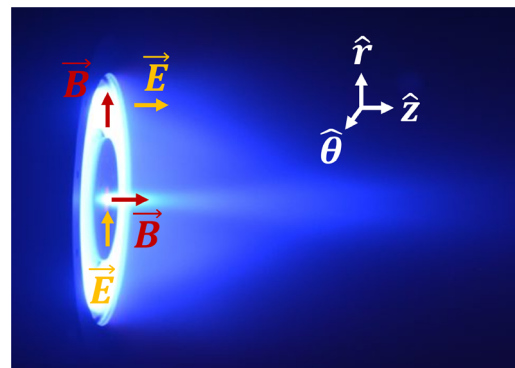


FIG. 1. Illustration of the electric and magnetic field at the acceleration channel and cathode, overlaid on a photograph of the H9 Hall thruster.

n_1 ; this phase lag leads to the growth of the instability at the expense of energy in the gradient-driven electron drift.

In practice, the anti-drift wave in a cylindrical plasma is a nonlocal wave, with discrete eigenmodes dictated by the azimuthal circumference of the plasma. The wave can then be described by azimuthal mode numbers $m \in \mathbb{Z}$, roughly corresponding to the Cartesian formulation via $m \approx k_y r$, where r is the radial coordinate. We show in Fig. 2 an example of high-speed footage capturing the anti-drift mode in a 6 kW Hall thruster, reproduced with permission from Ref. 23. In this image, the pixel brightness over time has been phase-correlated for frequencies in the range 70–90 kHz, so that the variation in phase with azimuthal angle demonstrates the global, $m = 1$ azimuthal propagation of the wave when viewed head-on. Langmuir probe measurements of Hall thrusters with central cathodes have shown that the anti-drift modes exhibit a maximum amplitude off axis, and propagate with fundamental frequencies on the order of 100 kHz with large-amplitude fluctuations, corresponding to >50% peak-to-peak variation in plasma density.²⁴

B. Impact of anti-drift waves on ion dynamics

The large amplitude and relatively low frequency of the anti-drift waves suggest they may be able to drive acceleration of the ions over longer timescales than the wave period. To quantify this effect theoretically, we develop in this subsection a simplified fluid model for nonlinear ion-wave interactions, with the goal of predicting the azimuthal ion properties of cathode-born ions as a function of the wave amplitude. While these wave-particle interaction processes are ultimately kinetic and we do not expect the ion population to reach equilibrium,

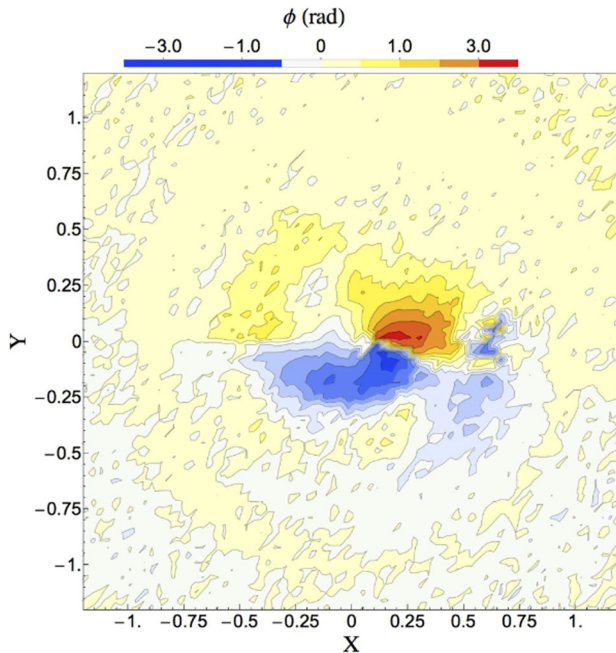


FIG. 2. Phase-correlated high-speed camera image demonstrating azimuthal propagation of the anti-drift mode in a 6-kW Hall thruster. Reproduced from Jorns and Hofer, *Phys. Plasmas* **21**, 053512 (2014), with the permission of AIP Publishing.

we focus on integrated fluid conservation equations to provide a simplified accounting of the bulk momentum and energy transfer between the wave structure and the ions. To accomplish this, we turn to the quasilinear approximation developed in Ref. 26. Following this approach, we perturb the ion velocity distribution function as $f(\vec{x}, \vec{v}, t) = f_0(\vec{x}, \vec{v}, t) + f_1(\vec{x}, \vec{v}, t)$, where f_0 is the component which evolves on a slow timescale relative to the wave frequency, and f_1 is the oscillating component. We likewise assume a corresponding electric field perturbation $\vec{E} = \vec{E}_0 + \vec{E}_1$. By phase-averaging the Vlasov equation over the wave period, we obtain

$$\frac{\partial f_0}{\partial t} + \vec{v} \cdot \nabla f_0 + \frac{e}{m} (\vec{E}_0 + \vec{v} \times \vec{B}) \cdot \nabla_v f_0 = -\frac{e}{m} \langle \vec{E}_1 \cdot \nabla_v f_1 \rangle, \quad (2)$$

where e is the ion charge, and m is the ion mass. This evolution equation for the slowly varying ion properties gains a source term on the RHS, corresponding to the effect of nonlinear wave rectification on the distribution function over many wave periods.²⁶ We have ignored the effect of classical ion collisions here in order to focus on the effects of the wave dynamics.

We then obtain the time-averaged ion density n_0 , velocity \vec{u}_0 , pressure tensor \mathbf{P}_0 , and internal heat flux \vec{Q}_0 by taking moments of the time-averaged distribution according to the conventions

$$\int f_0 d^3 v = n_0, \quad (3)$$

$$\int f_0 \vec{v} d^3 v = n_0 \vec{u}_0, \quad (4)$$

$$\int f_0 \vec{v} \otimes \vec{v} d^3 v = n_0 \vec{u}_0 \otimes \vec{u}_0 + \mathbf{P}_0/m, \quad (5)$$

$$\int f_0 \vec{v} v^2 d^3 v = \vec{u}_0 \left(n_0 u_0^2 + \frac{\text{Tr}(\mathbf{P}_0) + 2\mathbf{P}_0}{m} \right) + \frac{2\vec{Q}_0}{m}. \quad (6)$$

We may similarly define lowest-order perturbed fluid quantities based on the moments of the oscillating part of the distribution, yielding

$$n_1 = \int f_1 d^3 v, \quad (7)$$

$$\vec{u}_1 \approx \frac{\int f_1 \vec{v} d^3 v - n_1 \vec{u}_0}{n_0}. \quad (8)$$

Armed with this formulation, combining the zeroth and first moments of Eq. (2) results in the ion momentum conservation equation

$$m n_0 \frac{d\vec{u}_0}{dt} = e n_0 (\vec{E}_0 + \vec{u}_0 \times \vec{B}) - \nabla \cdot \mathbf{P}_0 + e \langle n_1 \vec{E}_1 \rangle. \quad (9)$$

The final term on the right-hand side represents the lowest-order time-averaged force on the equilibrium ion population from the wave's fluctuations in electric field and density. Similarly, we combine Eq. (9) with the next moment of the distribution to yield the quasilinear ion internal energy equation

$$\begin{aligned} \frac{1}{2} \frac{d(\text{Tr}(\mathbf{P}_0))}{dt} + \frac{1}{2} \nabla \cdot (\vec{u}_0 \text{Tr}(\mathbf{P}_0) + \mathbf{P}_0 \cdot \vec{u}_0 + 2\vec{Q}_0) \\ = \vec{u}_0 \cdot (\nabla \cdot \mathbf{P}_0) + e n_0 \langle \vec{E}_1 \cdot \vec{u}_1 \rangle. \end{aligned} \quad (10)$$

This relationship describes the evolution of the internal energy in terms of the pressure tensor. The second term on the RHS arises due to anomalous ion heating from work done on the ions by the wave electric field.

C. 1D model for cathode plume ion expansion

In order to compare predictions for wave acceleration and heating with experimental measurements of the singly charged ion properties of singly charged ions originating from the cathode plume, it is necessary to account for the trajectories of ions as they convect through the region of wave excitation. Focusing on cathode-borne ions, which traverse the inner front pole, we reduce Eqs. (9) and (10) to the radial direction, assuming cylindrical axisymmetry. These diverging ions must overcome a steep plasma potential well of ~ 15 V to leave the cathode plume in the radial direction.²⁴ As a result, only a small fraction of the ion velocity distribution at the cathode centerline possesses the energy to escape this well. While this is a fundamentally kinetic effect, we may apply our fluid formulation in Eqs. (9) and (10) to describe the subpopulation of ions which have sufficient radial velocity to overcome this barrier, simply by assuming they begin at cathode centerline with an initial radial velocity at or exceeding the well escape velocity.

A key measurable ion property of interest is the azimuthal ion velocity $u_{i\theta}$. The evolution of this parameter is described by the azimuthal component of Eq. (9),

$$u_{0r} \frac{du_{0\theta}}{dr} = -\frac{eu_{0r}B_0}{m} - \frac{e}{mr} \left\langle n_1 \frac{\partial \phi_1}{\partial \theta} \right\rangle - \frac{u_{0r}u_{0\theta}}{r}. \quad (11)$$

In Eq. (11), we have expanded the convective derivative in cylindrical coordinates, having assumed cylindrical symmetry such that the fluid properties are only functions of the radial coordinate, r . The first term on the right-hand side denotes the force imparted to the ions from the Lorentz force. We ignore the component of the azimuthal Lorentz force arising from the axial velocity, because ions that enter the pole region must have primarily radial velocities. The second term in Eq. (11) represents the quasilinear force from the anti-drift mode, which is a function of the amplitude and phase of fluctuations in both the plasma density and potential. We have invoked the electrostatic potential perturbation satisfying $\vec{E}_1 = -\nabla\phi_1$. The final term accounts for loss of azimuthal momentum to the radial direction as a result of the curvature of the cylindrical coordinate system.

In order to solve Eq. (11) for the azimuthal velocity, we must simultaneously solve for the evolution of the radial velocity u_{0r} , yielding the expression

$$u_{0r} \frac{du_{0r}}{dr} = \frac{e}{m} (E_r + u_{0\theta}B_0) - \frac{1}{mn_0} \frac{p_{0\theta}}{r} + \frac{u_{0\theta}^2}{r}. \quad (12)$$

In Eq. (12), the first term on the right-hand side represents acceleration due to the radial electric field and axial magnetic field, while the second term accounts for the divergence of the pressure tensor in cylindrical coordinates. Motivated by the fact that the azimuthally propagating anti-drift wave primarily impacts ion motion along that direction, we have assumed a diagonal but anisotropic pressure tensor with components p_{rr} , $p_{\theta\theta}$, and p_{zz} . We likewise assume that the wave dynamics primarily increase the spread of the azimuthal ion energy distribution, and thus $p_{\theta\theta} \gg p_{rr}, p_{zz}$. While we may define an effective azimuthal ion temperature via the relation $T_\theta = p_{\theta\theta}/(n_0k_B)$, we note that the ions are likely not in a thermodynamic equilibrium due to the large classical mean free path relative to the gradient length scale.²⁷ The final term is a centrifugal effect of the coordinate system, representing the fact that as an ion translates in a straight line, momentum

aligned to the azimuthal direction becomes more aligned with the radial direction.

The evolution of the azimuthal ion pressure, described by Eq. (10), can similarly be written in terms of the radial coordinate, yielding

$$\frac{1}{n_0} \frac{dp_{0\theta}}{dr} = -\frac{2e}{ru_{0r}} \left\langle u_{1\theta} \frac{\partial \phi_1}{\partial \theta} \right\rangle - \frac{p_{0\theta}}{u_{0r}r} \frac{d(ru_{0r})}{dr} - \frac{2p_{0\theta}}{r}. \quad (13)$$

In this expression, the first term on the right-hand side represents the change in pressure due to energy exchange with the wave. Since the sign of this term depends on the phase delay of the ion velocity fluctuation relative to the potential fluctuation, this term can represent either effective heating or cooling. The second term is a compressibility effect describing the decrease in pressure associated with radial expansion of the ions, while the third term accounts for the further decrease in density due to the increase in the cylindrical volume element with radius. We have ignored here the effect of the classical heat flux to retain tractability, since simple fluid approximations for this kinetic effect are likely not valid as a result of the large Knudsen number for expanding cathode ions.²⁷

Finally, in order to distinguish the effective azimuthal ion temperature from pressure via the relation $p_i = n_0k_B T_i$, we introduce a form of the ion continuity equation to solve for the ion number density,

$$\frac{1}{n_0} \frac{dn_0}{dr} = -\frac{1}{u_{0r}} \frac{du_{0r}}{dr} - \frac{n_0}{r}. \quad (14)$$

We note that the system of equations does not depend explicitly on the absolute ion pressure and ion density but instead on the relative changes in these quantities. We can therefore normalize each occurrence of the ion pressure and density in these expressions by the cathode centerline values, yielding the dimensionless quantity $\hat{n}(r) = n_i(r)/n_i(0)$ and the quantity $\hat{p}(r) = p_{0\theta}(r)/n_i(0)$ with units of energy.

The system defined by Eqs. (11)–(14) can be solved as an initial value problem in r , with the initial conditions representing the cathode centerline state of the subpopulation of ions, which are untrapped by the cathode plume potential well. To solve this system numerically, we require measurements of the near-centerline ion properties $u_{0\theta}(0)$, $u_{0r}(0)$, and $\hat{p}(0)$, in addition to the wave amplitudes \tilde{n}_1/n_0 , ϕ_1 , and $\tilde{u}_{1\theta}$ and electromagnetic field strengths E_r and B_0 . Note that by definition, the initial state of the normalized ion density $\hat{n}(0)$ is unity. We ultimately are able to leverage probe measurements from previous work on the cathode for the electric and magnetic field profiles.²⁴ However, we still require measurements of the wave perturbations as well as the background ion properties. By assuming that the azimuthal ion velocity is a sinusoidal fluctuation of the form $u(\theta, t) = u_0 + u_1 \cos(m\theta - \omega t)$, we can approximate the amplitude of plasma potential fluctuations from a simplified, Cartesian ion momentum equation on the fast timescale of the wave:

$$\phi_1(\theta, t) \approx \frac{m(\omega - k_0 u_{0\theta})}{ek_\theta} \tilde{u}_1 \cos(m\theta - \omega t) + O(u_1^2). \quad (15)$$

The first term is the result from linear theory, while the second, non-linear term is negligible provided that $u_1 \ll 2|\omega/k - u_0|$. In turn, we can estimate the amplitude of the plasma density fluctuations from the Boltzmann relation, yielding

$$\frac{n_1(\theta, t)}{n_0} \sim \exp \left\{ \frac{e\phi_1(\theta, t)}{k_B T_e} \right\} - 1. \quad (16)$$

These expressions ignore the phase delay between the density and potential fluctuations resulting from classical electron collisions—however, this phase delay is physically responsible for both the growth of the wave from the electron drift energy, as well as the transfer of momentum and energy to ions [c.f. Eqs. (11) and (13)]. For the purpose of our simplified model, then, we assume that the plasma density and potential are a quarter-cycle out of phase ($\pi/4$ radians), which maximizes these wave-particle interactions. This approximation allows for the evaluation of the time-averaged product in Eq. (11) as

$$\frac{1}{r} \left\langle \frac{n_1}{n_0} \frac{\partial \phi_1}{\partial \theta} \right\rangle \approx \frac{\omega k \phi_1}{2\pi} \int_{-\pi/\omega}^{\pi/\omega} \exp \left\{ \frac{\phi_1 \cos(\omega t)}{T_e} \right\} \cos(\omega t) dt, \quad (17)$$

where we choose $\theta = 0$ without loss of generality. This expression can be computed by numerical integration given only measurements of u_1 , T_e , and ω . Meanwhile, the product in Eq. (13) can be expressed as

$$\frac{1}{r} \left\langle u_{1\theta} \frac{\partial \phi_1}{\partial \theta} \right\rangle \approx \frac{u_1 \phi_1 k}{2}. \quad (18)$$

This framework provides a means for evaluating the impact of the wave from local measurements of the time-resolved azimuthal ion velocity. We describe in the following our technique for assessing this quantity in addition to the background ion properties.

III. EXPERIMENTAL SETUP

A. Test article and facility

In this study, we characterized the azimuthal ion velocities in the near-field cathode plume region of the H9 Hall thruster. The H9 is a 9-kW class Hall thruster with magnetic shielding and a centrally mounted cathode, developed as a laboratory test article through a collaboration between the Jet Propulsion Laboratory, the University of Michigan, and the Air Force Research Laboratory.²⁸ Figure 1 displays a photograph of the H9 operating. For this experiment, we fired the H9 on xenon propellant at a discharge power of 4.5 kW, corresponding to a discharge voltage of 300 V and a discharge current of 15 A. The thruster's body was electrically connected to the cathode. We carried out this test in Alec D. Gallimore Large Vacuum Test Facility (LVTF), the University of Michigan's 6-m-diameter by 9-m vacuum chamber.²⁹ The chamber was maintained at a xenon background pressure on the

order of 2 μ Torr during thruster operation, as measured by a Granville-Phillips Stabil ion gauge located in the exit plane of the thruster.³⁰

B. Optical bench for laser-induced fluorescence

In order to measure the local ion velocities, we implemented a laser-induced fluorescence (LIF) diagnostic. This technique makes use of a tunable diode laser to excite an electronic transition in a metastable state of singly ionized xenon, which subsequently decays to the ground state and spontaneously emits radiation of a different wavelength. By scanning the laser through a range of wavelengths and monitoring the intensity of fluorescence from the targeted transition, the Doppler-broadened line shape of the transition can be measured, which contains information about the ion velocity distribution of metastable ions along the laser injection axis. As is consistent with previous work,^{31–33} we assume that the velocity distribution of metastable states is representative of the ground-state velocity distribution on the timescales of interest (up to 100 kHz).³⁴

We show the experimental setup of our LIF system schematically in Fig. 3. Figure 3(a) displays the notional beam path on the optical bench, while Fig. 3(b) depicts the light injection and collection geometry with respect to the thruster. As can be seen from Fig. 3(a), we implemented a New Focus TLB-6716 tunable diode laser, which passed through a tapered amplifier to achieve up to 2 W of CW beam power. This laser supports a wavelength tuning range between 830 and 853 nm, which was chosen in order to excite the commonly targeted electronic transition in Xe II from the metastable $5p^4(^3P_2)5d^2[4]_{7/2}$ state to the $5p^4(^3P_2)6p^2[3]_{5/2}^o$ state at 834.953 nm in vacuum.³⁵ This excited state fluoresces at 542.06 nm in vacuum. We monitored the precise laser wavelength and relative beam power in real time by sampling a small portion of the beam energy into a wavelength meter and photodiode, respectively. We then modulated the beam in time to facilitate phase-sensitive detection with either a mechanical chopper or an acousto-optic modulator (AOM), as described further in the following. A 50–50 beam splitter divided the beam energy between these two modulation strategies.

An optical fiber transported the remainder of the beam power from either modulation apparatus to the vacuum chamber. This fiber was a multimode, 50- μ m-diameter step-index fiber with a numerical aperture of 0.22. A single 50-mm-diameter achromatic injection lens

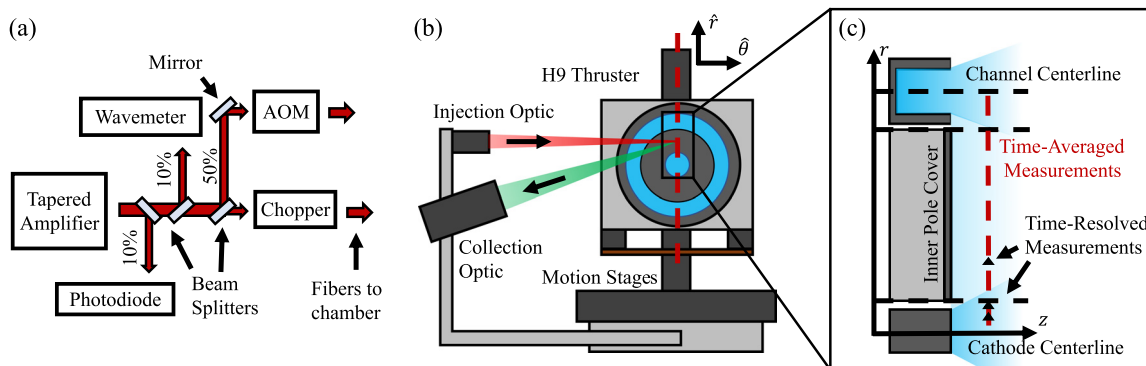


FIG. 3. Schematic of laser-induced fluorescence apparatus. (a) Optical bench light flow diagram. (b) Head-on schematic of LIF injection geometry. (c) Cross section view of thruster geometry with time-averaged and time-resolved LIF measurement locations (not to scale).

with a focal length of 100 mm then imaged the fiber at a spot in the thruster plume, with a magnification of ~ 10 such that the spot extended roughly 0.5 mm in size. This lens was placed such that the injected beam wavevector was aligned with the local azimuthal direction at the focus, as shown in Fig. 3(b). A dual-lens collection optic, consisting of two identical 75-mm-diameter achromatic lenses with $f = 200$ mm, imaged the spot from the injection optic onto the face of a larger collection fiber, spanning 1 mm in diameter with a numerical aperture of 0.39. This light was collected from an oblique angle out of the thruster plume.

The intersection of the focal regions of the two optics formed a 3D interrogation region about 1 mm^3 in volume, which defined the spatial resolution of the diagnostic. After transiting through the collection fiber, the photons originating from this volume passed through a narrow-band optical filter, which screened out stray plasma light at other wavelengths, after which the light impinged upon a photomultiplier tube (PMT), which converted the light intensity to electric current. In principle, the output of the PMT as a function of the input wavelength corresponds to the line shape of the target transition, for which the major shape-determining factor is Doppler broadening from the distribution of ion velocities along the laser axis.

We obtained spatially resolved measurements by mounting the H9 on a 3-axis motion stage. This allowed translation of the interrogation region in the $r - z$ plane of the thruster by shifting the vertical and axial motion stages. For this work, we maintained an axial position of 5 mm downstream of the exit plane, while translating the interrogation region from the cathode centerline $r = 0$ to the discharge channel centerline. Figure 3(c) displays a cutaway view of the $r - z$ plane with these measurement positions overlaid. We maintained optic alignment throughout testing by utilizing linear actuators to periodically realign visible lasers through the optics to an alignment reference, which was a 1-mm spot painted onto the front corner of the thruster's outer front pole cover with ceramic paste.

Background light from collisional excitation of the target transition and nearby transitions often obscures the signal of interest in laser-induced fluorescence experiments. To increase the signal-to-noise ratio (SNR), we used phase-sensitive detection (PSD), a signal processing technique which isolates the part of the signal that is modulated at the same frequency and phase as the laser beam modulation on the optical bench. While similar in principle, we employed slightly different methods for time-averaged and time-resolved PSD, respectively. For time-averaged LIF, a trans-impedance amplifier converted the PMT current to voltage, which was measured with an SRS 830 analog lock-in amplifier locked to the mechanical chopper frequency.^{36,37} In contrast, for time-resolved acquisitions, PSD was performed with post-processing software to realize the higher bandwidth offered by the increased chopping frequency of the AOM. In this case, the PMT current flowed through a 15-k Ω shunt resistor—a fast digitizer card then recorded the resulting voltage drop at a sample rate of 30 MS/s.^{31,32}

IV. ANALYSIS METHODOLOGY

We describe in the following our methodologies for extracting both time-averaged and time-resolved measurements of the ion properties from the LIF setup. In both cases, due to the low signal-to-noise of the excited signal, we employed denoising schemes based on phase sensitive detection.

A. Time-averaged laser-induced fluorescence

For our time-averaged measurements, we achieved phase-sensitive detection by modulating the beam energy with a mechanical rotary chopper at a frequency of 2 kHz. These measurements were effectively averaged over the lock-in time constant, $\tau_{\text{PSD}} = 300$ ms. The wavelength meter allowed a fine wavelength resolution of $\delta\lambda \approx 5$ fm. We employed the Doppler relation,

$$v = c \left(\frac{\lambda}{\lambda_0} - 1 \right), \quad (19)$$

to translate wavelength measurements to velocities, where v is the velocity component along the laser axis, c is the speed of light, λ is the laser wavelength in the lab frame, and λ_0 is the natural wavelength of the targeted transition. This yielded a velocity accuracy of 40 m/s. However, we used a standard velocity spacing of approximately 500 m/s to decrease measurement time. Typical values of signal-to-noise ratio ranged from 5 to 10.

Figure 4 shows an example of a time-averaged LIF spectrum, where wavelength has been converted to velocity in accordance with Eq. (19). The data points in this result are normalized to the maximum value for all of the time-averaged spectra. To avoid spurious effects in the analysis due to measurement noise, we fit the data with model curves representing either one or two Maxwellian populations (bold line in Fig. 4). We chose to use the sum of two Maxwellians for certain locations for which the measured spectra demonstrated asymmetric tails; however, no measured spectra showed wholly different, bimodal populations in this study. We propagated uncertainty from the fits using a Bayesian Markov chain Monte Carlo (MCMC) algorithm, which is discussed further in Ref. 38. Figure 4 displays 1000 samples of fits generated from this MCMC approach, demonstrating the portions of the velocity curve, which result in the greatest uncertainty according to this model.

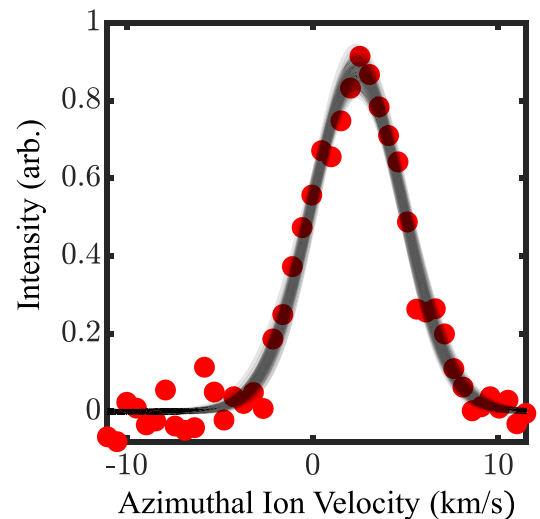


FIG. 4. Time-averaged ion velocity distribution obtained with laser-induced fluorescence at $(z, r) = (5 \text{ mm}, -r_K)$, where r_K is the keeper radius. Transparent curves represent samples from a distribution of bi-Maxwellian model fits to the experimental data obtained from Markov chain Monte Carlo sampling. The mean azimuthal velocity is 2.42 ± 0.08 km/s and the effective temperature is 8.5 ± 0.7 eV.

We integrated the fitted functions to compute the mean ion velocity and temperature, which are proportional to the mean and variance of the measured distribution:

$$\langle u_i \rangle = \int v f(v) dv / I, \quad (20)$$

$$k_B T_i = m \int (v - \langle u_i \rangle)^2 f(v) dv / I. \quad (21)$$

Here, we have defined the area under the distribution as

$$I = \int f(v) dv. \quad (22)$$

This quantity is proportional to the total light intensity collected by the PMT at all wavelengths. We computed uncertainties in the fluid parameters in Eqs. (20)–(22) based on the mean and 95% credible intervals from the sample set generated by the MCMC fitting algorithm.

B. Time-resolved laser-induced fluorescence

The use of a lock-in amplifier and mechanical chopper effectively averages the measurement over the integration time constant τ_{PSD} , so time resolution of faster fluctuations corresponding to frequencies $\omega > \tau_{\text{PSD}}^{-1}$ in the LIF signal is not possible with this technique. In order to extract time-resolved behavior on the timescale of interest for the azimuthal waves, we adapted an empirical transfer-function estimation technique developed by Lobbia for high-speed probing³⁹ and applied to LIF first by Durot.³¹

The empirical transfer-function LIF (TFLIF) approach constructs a linear, frequency-dependent mapping between the LIF fluctuations and a reference signal, which encodes the global plasma behavior. We used the thruster discharge current, measured with an inductive current probe, as this global reference. The laser was still chopped on the optical table, but at a frequency much faster than the sub-100-kHz oscillations of interest. We used an acousto-optic modulator (AOM) to modulate the laser intensity at 1.5 MHz. Phase-sensitive detection was then performed digitally in post-processing, with an effective time constant of $\tau_{\text{PSD}} = 700$ ns. Following this, we estimated average transfer functions relating the discharge current trace to the LIF signal at each wavelength and location. This was accomplished by breaking each 30 s signal acquisition into many smaller chunks, and dividing the discrete Fourier transform (DFT) for each chunk by the DFT of the corresponding discharge current trace for each wavelength. The transfer function for each chunk was then averaged to reduce noise effects. We repeated this algorithm for ~ 20 wavelengths, corresponding to an azimuthal velocity range of $|v_\theta| < 10$ km/s, which led to a velocity spacing of 1 km/s.

The LIF signal and reference discharge current data were streamed in real time from an AlazarTech ATS9462 digitizer card at 30 MS/s, where they were stored as 16-bit binary data on a solid-state storage drive. This generated roughly 2 GB of raw data per transfer function, corresponding to 40 GB per position for each full 20-velocity IVDF dataset. We then synthesized time-resolved LIF traces from a common discharge current reference trace by inverting the estimated transfer functions for each velocity–position combination. This process generated an ensemble of simultaneous LIF measurements at each velocity and wavelength, based on the linear frequency-domain mapping between discharge current fluctuations and the ion velocity

distribution fluctuations. We down-sampled the resulting time-resolved IVDF data in time by a factor of 20 to an effective sample rate of 1.5 MS/s to reduce the data size, and applied a two-Maxwellian best-fit to the IVDF at each time step to reduce noise effects, in the same way as the time-averaged data. We show in Sec. V both these time-resolved IVDFs and their moments, which are calculated following the prescription from Sec. IV A.

V. RESULTS

In this section, we present measurements of the azimuthal ion velocity distribution near the cathode plume of the H9 Hall thruster obtained with the laser-induced fluorescence diagnostic. We begin by showing the time-averaged measurements, which represent background ion properties averaged over any oscillatory behavior. Following this, we examine time-resolved data to investigate the wave behavior, which may explain the anomalous features of these background properties.

A. Time-averaged ion dynamics

Figure 5 displays the results of time-averaged LIF for the azimuthal ion velocity distribution function (IVDF) at an axial distance of 5 mm from the thruster exit plane. We show ion properties as a function of radial position across the thruster face, ranging from the cathode centerline to the center of the discharge channel. Radial distances are normalized to the keeper radius r_K .

In Fig. 5(a), we display contours of the IVDF as a function of radial position. Each vertical slice corresponds to the velocity distribution along the azimuthal direction at that location. We normalize the height of the distribution to the maximum light intensity at each position in order to highlight the change in shape of the distribution. The distance between the mean velocity of the distribution and the horizontal axis is indicative of net azimuthal ion drift speed, i.e., swirl. In addition, the breadth of the distribution along the azimuthal direction, which is described by the effective azimuthal ion temperature, increases significantly off of cathode centerline. The combination of increased drift speeds and high ion temperatures lead to elongated tails in the IVDF, extending to ion velocities exceeding 5 km/s at locations between 1 and 5 keeper radii, corresponding to the entire inner front pole surface [see Fig. 3(c)]. These features suggest the presence of a mechanism accelerating and heating the ions close to the inner front pole.

To quantify this effect more explicitly, we show in Figs. 5(b)–5(d) the moments of the distribution at each location including the intensity [Eq. (22)], the mean velocity [Eq. (20)], and the temperature [Eq. (21)], respectively. On these plots, we mark the locations of the cathode centerline, inner pole inner radius, and inner pole outer radius with vertical lines, as shown in Fig. 3(c). Figure 5(b) demonstrates that the light intensity from the LIF emission is relatively low in front of the cathode, compared to the pole region, which is more intense than the cathode by a factor of 2–3. Furthermore, the LIF signal at the outer edge of the inner pole is roughly 6–14 times brighter than directly in front of the cathode plume. Since the cathode plasma is known to have the highest plasma density of these regions due to the low-velocity flow through the cathode orifice, the time-averaged LIF intensity we see is not representative of the overall plasma density. This may be explained by the fact that the amount of light collected by LIF is the result of a balance of collisional-radiative processes, by which electrons

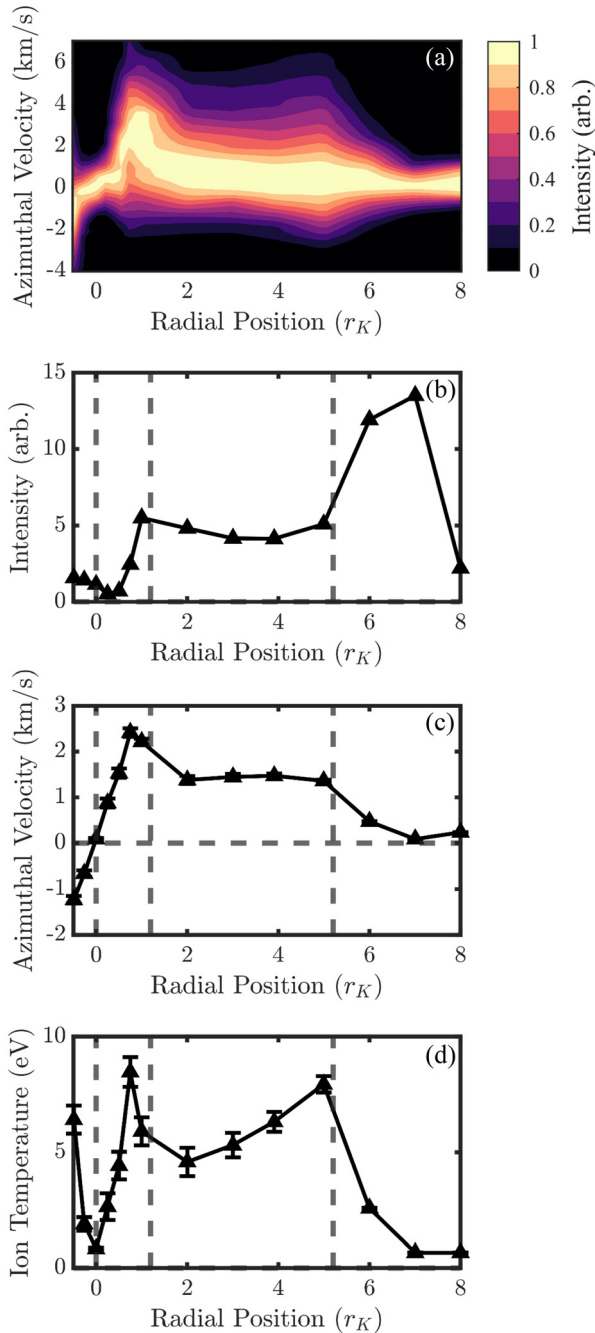


FIG. 5. Ion fluid properties 5 mm from the thruster exit plane measured with time-averaged LIF. (a) Azimuthal ion velocity distribution function normalized to maximum. (b) Total light intensity. (c) Mean ion azimuthal velocity. (d) Ion temperature.

excite the metastable state targeted by the laser at a rate dependent on the electron temperature and spectral selection rules. It thus is dependent on several features including ion residence time, local electron temperature, and density. The convolution of these factors can give rise to intensity profiles that deviate from the local density.

Figure 5(c) shows the mean azimuthal ion velocity at each radial location. While ions exiting the cathode at $r = 0$ have little drift velocity (as required by cylindrical symmetry), the cathode ions begin to drift azimuthally at greater r values. The azimuthal swirl speed approaches a maximum of 2.5 km/s near the keeper edge ($r = 1r_K$), before falling to an intermediate value of 1.5 km/s across the inner front pole. This azimuthal drift is mirrored across the cathode centerline with negative velocities at negative radii, which is consistent with a global rotation of the ion population in the cathode plume and pole region. These swirl velocities agree with previous measurements performed on tests of standalone magnetized hollow cathodes,³⁸ demonstrating that this behavior remains present in the more complex plasma environment of an operating Hall thruster.

Finally, in Fig. 5(d), we display the azimuthal ion temperature. Similarly to the mean ion velocity, the ion temperature quickly grows from a low value of approximately 1 eV on the cathode axis as ions expand outward, reaching a peak of nearly 9 eV near the keeper edge ($r = 1r_K$). The ion temperature then exhibits a local minimum of 5 eV in front of the inner pole before again rising to a large value of 8 eV at the outer edge of the inner pole. Moreover, we note that in some cases, as shown from the IVDFs in Fig. 5(a), the high-velocity tail of the distribution is elongated with velocities/energies exceeding 5–7 km/s (~ 30 eV of kinetic energy). These temperatures and corresponding outlier ion velocities are unlikely to be caused by classical processes such as the time-averaged electrostatic and collisional forces on the ions, instead representing a major departure from commonly assumed ion temperatures of 1–2 eV in the cathode plume.⁴⁰

Taken together, the existence of large ion swirl velocities and temperatures is notable as discussed in the preceding, because ions which fall through the pole cover sheath may impact the surface with higher kinetic energies and steeper angles of incidence than expected from classical mechanisms. The combination of these effects could promote enhanced erosion of such surfaces, reducing component lifetime. We further discuss the implications of these high ion energies on thruster erosion and lifetime in Sec. VI. Physically, it is likely that the mechanisms producing these unexpectedly high ion temperatures and velocities at the keeper/pole interface are related. In order to investigate possible causes for these large energies, we turn in Sec. VB to time-resolved measurements of low-frequency oscillations in the ion properties.

B. Time-resolved ion dynamics

In Fig. 6, we present time-resolved LIF measurements of the azimuthal IVDF. Each column of plots in Fig. 6 contains data from different radial locations at a distance of 5 mm downstream of the H9 exit plane: the keeper face ($r = 0.5r_K$), the keeper/pole interface ($r = 1r_K$), and the inner pole ($r = 3r_K$), respectively. The first row [Figs. 6(a)–6(c)] displays the contours of the azimuthal IVDF over time. These simultaneous IVDFs are synthesized from a single discharge current trace using the transfer-function averaging technique described in Sec. III. In these plots, each vertical slice is normalized to the time-averaged intensity in that location, such that the coloring reflects the relative fluctuations in the height and shape of the distribution. Figure 6 also displays the time-resolved LIF intensity [Eq. (22)], mean velocity [Eq. (20)], and ion temperature [Eq. (21)], respectively, inferred from the moments of the time-resolved traces from Figs. 6(a)–6(c). The final row in Fig. 6 contains discrete Fourier

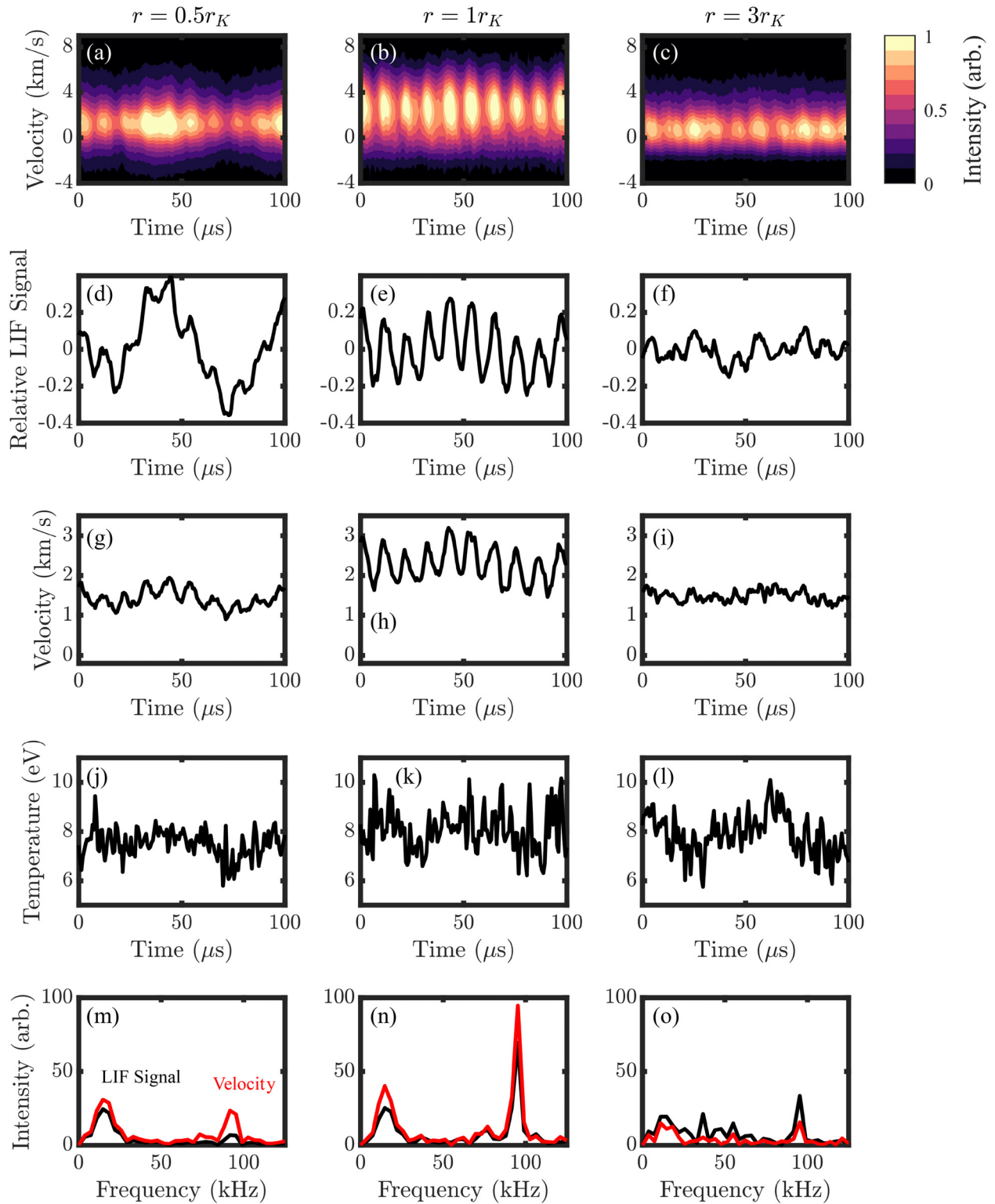


FIG. 6. Time-resolved ion properties, including IVDF shape (a)–(c), total LIF intensity (d)–(f), mean velocity (g)–(i), and ion temperature (j)–(l), along with the Fourier transform of the intensity and velocity curves (m)–(o). The three columns represent data at $r = 0.5r_K$, $r = 1r_K$, and $r = 3r_K$, respectively.

19 August 2024 13:59:35

transforms of the intensity and velocity to demonstrate the relative contributions of different frequency ranges to these fluctuations.

The oscillations in the IVDF intensity and shape in Figs. 6(a)–6(c) demonstrate frequency content at 20 and 90 kHz across the thruster face. The lower-frequency content is likely associated with the breathing mode, which is a global discharge current oscillation driven by ionization instability in the Hall thruster channel that is typically observed at 10–25 kHz.⁴¹ We infer that the additional oscillation at 90 kHz results from the anti-drift mode, which was previously measured to occur at this frequency in the H9 with time-resolved probing techniques.²⁴ At the first location in front of the keeper face [$r = 0.5r_K$, Fig. 6(d)], the LIF intensity has the largest total amplitude, with a peak of 40% the background value. This variation is dominated [Fig. 6(m)] by the lower, breathing mode frequency. There is a contribution to the intensity fluctuations from the higher-frequency mode at 90 kHz, as exhibited by the smaller amplitude variations superimposed on the lower-frequency oscillation. These variations are also captured by the Fourier transform [Fig. 6(m)]. In terms of velocity, it appears that at this location, both modes contribute to variations in the azimuthal speed. This is manifest in Fig. 6(g) as higher-frequency variations in velocity superimposed on a lower-frequency undulation. Notably, the contribution of the 90 kHz mode to velocity variation is comparable to the breathing mode [Fig. 6(m)] despite the fact the intensity fluctuations are smaller.

The amplitude of the 90-kHz oscillations in velocity and intensity becomes more pronounced than the breathing mode contribution at the pole-keeper interface ($r = 1 r_K$). This manifests as a stronger high-frequency component to the oscillations in Figs. 6(e) and 6(h), which demonstrate primarily sinusoidal behavior. Meanwhile, the fluctuations in front of the pole at $r = 3r_K$ are less coherent, with the frequency content spread out over a wider range of frequencies. The spectra suggests the breathing mode and anti-drift wave remain but at reduced amplitude. At all locations, variations in the ion temperature are dominated by noise and do not demonstrate significant contributions from these frequency components. This may be due to a large dependence of the temperature on the high-energy tail of the distribution, which appears to be more susceptible to spurious, high-frequency noise due to fitting uncertainty in Figs. 6(a)–6(c). We note that the time-resolved temperature values at $0.5r_K$ and $3r_K$ exceed the temperature associated with the time-averaged IVDF [Fig. 5(d)]. However, artificially taking the time average of the measured time-resolved IVDF generally agreed well with the time-averaged measurement. This discrepancy may then result from the fluctuations in the IVDF. The time-averaged temperature in Fig. 5(d) quantifies the effective width of the time-averaged IVDF, which depends on fluctuations in the velocity and plasma density. Because of the nonlinear nature of the second moment calculation [Eq. (21)], we would therefore not necessarily expect the time average of the time-resolved temperature to agree with the time-resolved temperature.

These observations are consistent with a physical understanding of the plasma oscillations in the thruster. The breathing mode is characterized by variation in the total discharge current (a feature stemming from its relation to ionization), which is primarily carried along axial field lines by electrons in the cathode plume. This variation in current density agrees with the large variation in ion density suggested by the LIF intensity fluctuations near the cathode, which decreases in amplitude with radial position. The impact on azimuthal velocity from

the breathing mode is expected to be indirect, perhaps stemming from variations in electric field contribution to moderate Lorentz force effects. This explains why this mode is correlated with strong intensity fluctuations, while it is only moderately correlated with velocity fluctuations. Meanwhile, the anti-drift mode results in azimuthal electric field oscillations.²³ The correlation may elucidate why this mode appears to contribute more strongly to the velocity fluctuations at the innermost location even though the intensity fluctuations are muted compared to the breathing mode. Moreover, the anti-drift wave has its peak amplitude off-centerline due to its cylindrical structure. This is consistent with our observation of a maximum in the amplitude of velocity and ion density oscillations at the edge of the cathode keeper.

Significantly, we also note that the time-averaged swirl velocity and ion temperature are both maximized in a location nearby this measurement of large wave amplitudes (Fig. 5), which suggests correlation that this 90-kHz wave behavior may be tied to the large ion energies apparent in the background IVDF. Armed with this insight, we turn to Sec. V C to determine if there is a theoretical link between the time-resolved and time-averaged behavior.

C. Evaluation of 1D model with experimental measurements

In order to quantify the effect of the anti-drift mode on the azimuthal ion properties, we evaluated the 1D model for the radial evolution of ion velocity developed in Sec. II. This model required experimental inputs for the axial magnetic field profile as well as the amplitude profile of the anti-drift mode. To this end, we show in Fig. 7(a) the normalized axial magnetic field as a function of radial coordinate at an axial location of 5 mm from the thruster face. We obtained this field map from a COMSOL simulation of the thruster magnetic circuit, which was validated against Hall probe measurements. Previous Langmuir probe measurements taken further downstream suggest that there is an inward-pointing electric field at small radii, with very little radial electric field beyond $r > 0.4r_K$.²⁴ We imposed a radial potential gradient interpolated from those measurements, also shown in Fig. 7(a). While these measurements only extend out to two keeper radii, the potential asymptotes to a nearly constant value of 26 V; we therefore extrapolate this value out to larger radii within the simulated domain. We then specify an initial radial velocity for the ions on the cathode centerline. While the thruster symmetry dictates that the true mean velocity vanishes on the axis, this initial speed allows us to account for the small subpopulation of ions with sufficient thermal speed to escape the cathode potential well.

We show in Figs. 7(b)–7(d) experimental measurements of the amplitude of fluctuations in azimuthal ion velocity, $|u_1|$, plasma potential, $|\phi_1|$, and density, $|n_1|/n_0$. We determined the amplitude of the ion velocity fluctuations associated with the anti-drift wave [c.f. Figs. 6(g)–6(i)] by applying a numerical high-pass filter with a cutoff frequency of 50 kHz to the 270- μ s time series and taking the root mean square. The filter served the purpose of eliminating the contribution of the lower-frequency breathing mode oscillations to the overall amplitude. As described with the relations in Sec. II C, once we had the velocity fluctuation amplitude, $|u_1|$, we could infer the remaining wave amplitude quantities ($|n_1|/n_0$ and $|\phi_1|$). We note that in order to compute the density fluctuation amplitude, $|n_1|/n_0$, from the velocity data using Eq. (16), we required an assumption for the electron temperature, T_e , which was not measured in this work. We generated the

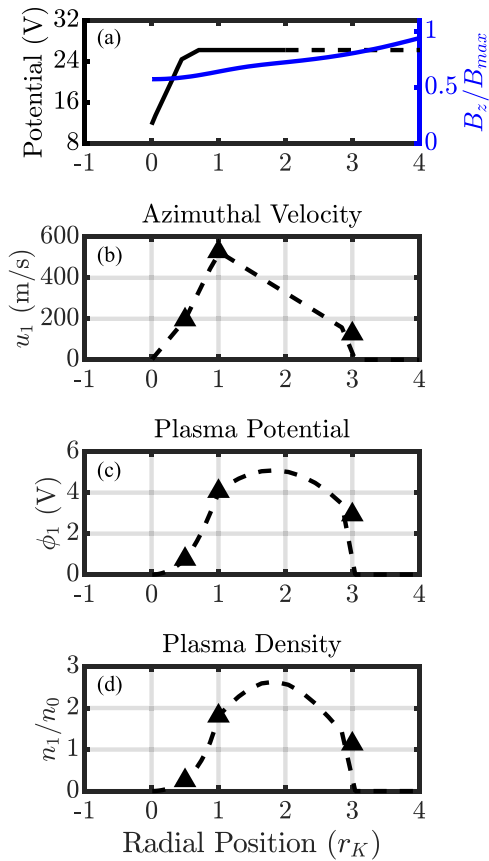


FIG. 7. Input parameters for the radial ion velocity model. (a) Axial magnetic field (normalized to maximum) and plasma potential in the vicinity of the cathode according to Langmuir probe measurements.²⁴ The dashed line shows a constant extrapolation of the potential profile. (b)–(d) Amplitude of plasma parameter fluctuations [(b) velocity, (c) potential, and (d) density] inferred from the time-resolved azimuthal ion velocity measurements, interpolated linearly (dashed lines).

density fluctuation amplitude values in Figs. 7(b)–7(d) assuming a value of $T_e = 3$ eV, which is consistent with Langmuir probe measurements of similar cathodes.⁴⁰ However, to integrate the model we sampled from a range of electron temperature values, which we describe further in the following. In practice, we only performed TFLIF measurements at three interrogation region locations due to the long acquisition time associated with the diagnostic. To generate a continuous wave amplitude profile for evaluating our model, we thus used a linear interpolation scheme to estimate u_1 at r values between the measurement locations. The nonlinear dependence of the resulting potential and density amplitudes on r stems from the functional form of the azimuthal wavenumber $k \approx 1/r$.

Armed with these experimental measurements, we integrated the system of four equations [Eqs. (11)–(14)] numerically using a fourth-order Runge–Kutta algorithm. We specified the initial state of the ions at a small radial coordinate of $r = 0.1$ keeper radii to avoid numerical singularities at $r = 0$. The ions were initialized with zero azimuthal velocity and a temperature of 1 eV—corresponding to the time-averaged LIF measurements of ion properties on cathode centerline. In

our formulation, we treated both the electron temperature T_e and initial radial ion velocity, u_{0r} , as uncertain parameters. This stems from the fact that we did not have direct measurements of these quantities in this work. In order to capture the impact of this uncertainty, we generated a set of 1000 random samples from uniform distributions within the parameter ranges $T_e \in (1, 3)$ eV and $u_{0r} \in (4.8, 5.2)$ km/s. These ranges are consistent with measurements previously performed on similarly-configured cathodes.^{40,42,43} The mean initial radial velocity of 5 km/s approximates the minimum “escape velocity” of the ~ 15 V cathode potential well. The small fraction of thermal ions on cathode centerline, which meet this condition for escape must be concentrated around this velocity. We then evaluated the model for each sample of parameters, resulting in an approximate empirical probability distribution over the model output quantities. In the following discussion, we present the median and central 70% credible interval from this analysis.

Figure 8 displays a comparison between the numerical solution of the 1D ion acceleration model and the mean ion properties measured with time-averaged LIF. We evaluated the model for two scenarios: with and without the wave-based heating and forcing terms. The latter case represents the “classical” effects based only on the Lorentz force. However, we note that we have neglected the component of the Lorentz force due to axial ion motion, which is assumed to be small for ions which escape the cathode radially and traverse across the inner front pole [c.f. Eq. (11)].

For this classical case, we see in Fig. 8(a) that the ions begin close to cathode centerline with zero azimuthal velocity. However, the ion swirl gradually increases with radius due to the Lorentz force from the axial magnetic field. This classical profile, however, fails to capture both the location and the magnitude of the experimental peak in azimuthal ion velocity, which is located close to $1r_K$. Finally, the wave acceleration model exhibits a subtle inflection in the azimuthal ion velocity of about 1 km/s, which is qualitatively similar to the measured profile in that region. The measured velocities still exceed those predicted by the model by up to a factor of 2.5, however. Physically, this result demonstrates that the presence of anti-drift waves are energetically capable of accelerating ions to swirl velocities exceeding 1 km/s in the near-field cathode plume, although we note that neither the classical model nor the wave model fully captures the rapid ion acceleration at small radii. We omit measurements beyond 5 keeper radii, corresponding to the approximate location at which ions predominantly originate from the thruster channel rather than the cathode. We return to a discussion of possible causes of these discrepancies between the model and experiment in Sec. VI.

Figure 8(b) shows the model predictions of ion temperatures against the LIF values. Since the classical case (without wave effects) includes no heating mechanism, the classical ion temperature falls quickly to zero from the “initial” centerline value as the ions expand radially. The classical temperatures are therefore not visible in Fig. 8(b). In contrast, the numerical model shows wave heating of the ions to peak values ranging from 10 to 12 eV. The size of the simulated temperature increase agrees with the LIF measurements, although the first peak in measured ion temperature occurs closer to the cathode centerline, near $r = 1r_K$, than the simulated peak in temperature at $2r_K$. In addition, the measured ion temperature profile displays a second peak near $r = 5r_K$, which is not predicted by the ion heating model. The discrepancies between model and experiment again may

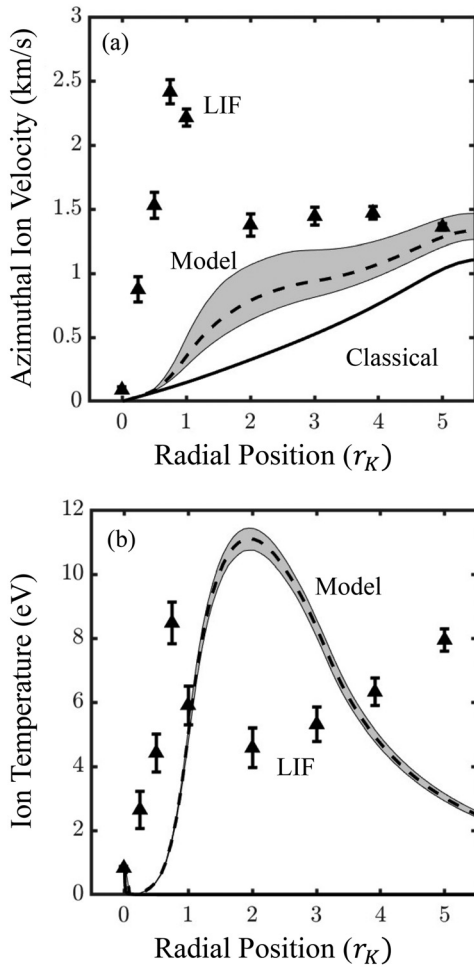


FIG. 8. Comparison of time-averaged LIF data with results from the radial ion acceleration model. The dashed line represents the median of the ensemble of model evaluations, with error bounds demonstrating the 70% credible interval. (a) Azimuthal velocity. (b) Ion temperature.

in part be attributed to the simplifications we invoked in the model (see Sec. VI). With that said, the fact that the model can qualitatively reproduce these ion temperature results suggests that the anti-drift mode possesses sufficient energy to at least partially explain high ion temperatures in the near-field cathode plume. The cooler ions at larger radii in the model solution can be physically attributed to the radial expansion of the ions after leaving the region of wave activity, as well as the neglect of channel ions, which likely dominate for $r > 5r_K$.

In summary, although there are differences between the experimentally informed model for the ion dynamics and the time-averaged measurement, our results ultimately demonstrate that the anti-drift mode is likely an important driver for the azimuthal ion energies in the cathode plume region. We discuss the implications of this finding in Sec. VI.

VI. DISCUSSION

In this work, we have presented direct measurements of non-classical azimuthal ion energies in the cathode plume and inner pole

region of an operating Hall thruster. We discuss in the following the relationship of this result to previous findings, the physical processes driving the azimuthal dynamics, and the implications of these results for our understanding of erosion of the near-pole.

A. Relationship of results to previous studies

Our results, which have focused on the azimuthal ion dynamics, are consistent with previous studies and hypotheses related to the near-field cathode and pole region in Hall thrusters with a center-mounted cathode. In particular, this observation of non-classical ion velocities and temperatures is preceded by our similar measurements of energetic ion swirl properties in standalone tests of the AEPS cathode.³⁸ Our work extends this finding by demonstrating that these effects remain in a full Hall thruster discharge. Additionally, the existence of non-classical azimuthal velocities was anticipated by theoretical arguments presented in Refs. 42 and 18 regarding the possible existence of swirl in the cathode plume. This previous work showed the existence of outward radial acceleration of the ions near the cathode. This was unexpected classically, given the fact that the local electric field points radially inward. It was suggested in this work that there must be some other effect—namely, azimuthal acceleration—which increases radial velocities due to the centrifugal force. Our work shows conclusively that such a swirl exists and can explain radial expansion at multiple km/s. In a departure from this previous finding, where it was suggested that microturbulent acoustic waves drive the ion swirl, our results show that lower-frequency, rotational waves may also play a role in the azimuthal ion swirl and heating.

B. Limitations of methods

We have presented in the preceding a theoretical model to explain—at least in part—the physical processes driving the anomalous swirl and heating of the cathode and pole ions. We have shown based on our time-resolved measurements that the presence of the 90-kHz anti-drift wave, which was previously linked to anomalous electron transport,²⁴ may also explain the increase in ion energy and velocity in this region. Physically, this results because of a transfer of momentum and energy from the gradient-driven electron drifts in the azimuthal direction to the ions, mediated through the excitation of this coherent, large-amplitude, azimuthal wave. Indeed, it appears this mechanism can qualitatively explain key trends for both the increase in swirl and azimuthal temperature as ions expand from the cathode, as shown from the results of our 1D acceleration and heating model in Fig. 8.

With that said, we note that the model predictions do not directly match the data. As we alluded in Sec. VI A, this may in part be attributed to the simplifications invoked in our derivation of the governing equations. For example, the most notable disagreement between the model and the LIF data is that the actual ions experience much more intense acceleration and heating close to cathode centerline than predicted. In contrast, the model profile shows more gradual acceleration, and even though the simulated heating occurs rapidly, its location is displaced by at least $+0.5 r_K$ compared to the experimental data. We note that the rapid decrease in velocity and temperature from $r = 1r_K$ to $r = 2r_K$ can be qualitatively explained by the centripetal terms in Eqs. (11)–(14), which account for the transfer of azimuthal momentum into radial momentum due to the curvilinear coordinate system. However, the amplitude of the excitation which we estimate from the

data is not intense enough to yield the height of the peaks in these quantities at $r \sim 0.9r_K$. It is therefore clear that the mechanism for this rapid ion energization near centerline must be very intense and localized near the cathode axis. Furthermore, we note that the simulated ions increase in velocity monotonically with radial position—this is due to the classical acceleration by the axial magnetic field. The measured velocities instead remain nearly constant from $2r_K$ to $5r_K$, which is likely a superposition of this classical acceleration with the more intense anomalous acceleration and which results in the peak velocity near centerline.

One possibility is that our interpolated wave amplitude profile [c.f. Figs. 7(b)–7(d)] does not capture the peak in the wave intensity. If, for instance, our relatively sparse measurements of the wave amplitude have missed the location of a larger peak amplitude, between 0.5 and $1 r_K$, the ions could experience more intense acceleration and heating. We also note that our model predictions depend sensitively on the radial speed of the ions, which effectively dictates how much time the ions spend being acted on by the wave fields. While our model has targeted the subpopulation originating from the cathode centerline, which already possess sufficient velocity to escape the potential well there, other trapped ions could also gain this escape energy. This escape could occur due to random velocity-space shuffling arising from classical collisions, or even from the action of the wave itself on trapped ions. Furthermore, we note that the large amplitude and global nature of these waves suggests that not only do the waves exert nonlinear forces on the particles, but also that the saturated state of the waves themselves may differ significantly from the linear theory we have described. For example, our calculations in Fig. 7(d) suggest that the plasma density may vary by more than a factor of two, whereas the dispersion relation of the anti-drift mode is derived under the assumption that $n_1/n_0 \ll 1$. While our wave acceleration calculations are based on measured amplitudes and thus do not directly depend on the wave perturbation staying in a linear regime, these large electric fields could lead to strongly nonlinear behavior, such as wave–wave coupling or particle trapping, which may alter the macroscopic force on the ions. Taking into account for such effects in full would require a kinetic treatment of ion momentum and energy transport but could play a major role in quantitatively explaining the steep ion acceleration curve within this potential well.

Another source of disagreement arises from the fact that the quasilinear model wholly neglects channel ions, whereas in reality the plasma in front of the pole is made up of a combination of ions originating from both the cathode plume and discharge channel. We especially expect the channel ions to play more of a role at larger keeper radii ($r \gtrsim 4r_k$), where we observe lower azimuthal temperatures and velocities associated with the beam population. Additionally, the second peak in ion temperature at $5r_K$, which is not represented by our model, could be a result of a separate heating mechanism related to the channel ions. For example, it has been proposed that higher-frequency instabilities driven by these counterstreaming ion populations may play a role in the pole ion dynamics;^{18–20} The frequency bandwidth of the time-resolved LIF diagnostic applied herein exhibits strong attenuation for frequencies above 100 kHz, so it is possible that such instabilities are present but undetectable by this diagnostic. On a related note, it has been suggested that ion acoustic turbulence, which primarily propagates in the longitudinal direction, is still able to transfer azimuthal electron momentum to the ion population through effective

collisions.¹⁸ If present, this effect could partially explain the differences in the anomalous acceleration profile and the model (Fig. 8). Additionally, other work has suggested that a resistive MHD mode is present in higher-current cathodes, with the similar character to the anti-drift mode ($m = 1$, <100 kHz).^{44,45} While that work predicts the onset of such behavior at larger discharge currents than we investigated in this study, it is possible that this electromagnetic behavior occurs in addition to the electrostatic modes that we have focused on. The superposition or interaction of these two rotational effects could further mediate energy and momentum transfer to the ion population. Another simplification is that our model only accounts for radial ion motion. The motion of ions in the axial direction may reduce the residence time in the regions of high wave amplitude, as well as lead to the properties depending instead on the plasma properties at other axial positions. We expect this also could impact the effective power and momentum balance and therefore shift the shape and magnitudes of the predicted velocity and temperature profiles.

As a final consideration, we remind the reader that our approach has ignored the effects of classical ion collisions with neutrals, electrons, and other ions. The mean free paths for these interactions are larger than the gradient length scales in the plume plasma—therefore, the flow is at least in a transitional, if not rarified, regime. However, while the probability of ion–electron collisions is exceedingly low, the results of collisions with neutrals may not be negligible for the ions. This is especially the case near the cathode exit, where the neutral density is large.²⁷ In particular, including neutral scattering in the description of near-cathode physics would result in a drag force on the ions, serving to reduce the effect of wave acceleration and potentially exchange this directed energy for random thermal motion, allowing for further heating. Furthermore, complicating matter is the internal heat flux, which arises from the skewness (third moment) of the IVDF. In a sufficiently collisional regime, this term in the energy equation can be approximated using a Fourier law (i.e., $\vec{Q}_0 = -\kappa \nabla T_i$, where κ is a collision-rate-dependent thermal conductivity) stemming from small collisional perturbations to the equilibrium distribution function. Including this effect would serve to smooth out temperature gradients and reduce the peak ion temperatures in the model prediction. However, this approximation likely breaks down for cathode ions in front of the pole due to their long mean free paths, in which case the heat flux can be nondiffusive and nonlocal, having sensitive dependence on the boundary conditions.^{46,47} To capture this fundamentally kinetic energy transport accurately, more sophisticated models are necessary. Both neutral and ion collisions could also lead to some degree of self-equilibration, tending to distribute the intense azimuthal ion energies in the radial and axial directions as well. While these collisional effects would be key to obtaining a high-fidelity accounting of the pole ion dynamics, the fact that we observe such severe temperature gradients and large azimuthal speeds suggests that the effects of collisions, which would reduce these values, are secondary to the anomalous acceleration and heating, and therefore are beyond the scope of this study. Despite these limitations, this simple model demonstrates that the conditions in the near-field cathode plume are favorable for significant transfer of energy and momentum from the electron drift to the ions through both bulk acceleration and heating via the anti-drift mode.

In addition to this discussion of model assumptions, we must also consider the limitations of our experimental techniques. In this

work, we have assumed that the observed broadening of the targeted line shape accurately represents the shape of the ion velocity distribution. However, other effects may generally contribute to line broadening, such as state splitting due to fine and hyperfine structure, the Zeeman effect in the presence of magnetic fields, and the Stark effect in the presence of electric fields.³⁶ While a full consideration of these atomic line broadening mechanisms is beyond the scope of the present work, we echo the arguments of Refs. 13 and 37 in concluding that such effects represent only a small error to the relatively large estimated ion temperatures, and virtually no error for the mean ion velocities.

We have also assumed that the dynamics of ions in the metastable state of Xe II that is directly accessed by our diagnostic are representative of the ions as a whole, despite the fact that the majority of ions are in the ground state. Collisional-radiative models for xenon suggest that this is a reasonable assumption even for the 100-kHz time scales investigated here;^{34,48} however, care is required in interpreting the fluctuations of intensity in time-resolved LIF data as well as the impact of charge-exchange effects. For example, variations in the electron temperature or neutral density which trigger fluctuations in collisional excitation of this metastable state could in turn induce perturbations to the brightness of the fluorescence signal. As a final note, the inferences we make based on this diagnostic only apply directly to the singly ionized xenon species. While species of higher ionization state likely compose only a small fraction of the heavy particles in the pole region,¹⁴ the electrostatic wave acceleration and heating mechanisms which we have investigated in this work arise from terms which scale with ion charge. Therefore, these effects would produce even greater energy addition to any higher charge states present, further increasing the impact of the anti-drift mode on ion energization.

C. Implications for Hall thruster pole erosion

As discussed in the introduction, one of the motivations for this work is to elucidate the role of azimuthal dynamics in energetic ion production in the near-field plasma in a magnetically shielded Hall thruster's front pole region. Previous studies have shown that ion bombardment of the inner front pole is the primary lifetime-limiting mechanism of this class of thruster.^{6,14,25} While classical fluid models have shown that in some cases, this bombardment can be attributed to energetic ions originating from the channel; in others, it has been suggested that there must be a non-classical heating mechanism for the ions in this region.^{16,17} Modeling results, for example, have considered the possibility that anomalous heating effects arise from high-frequency (>1 MHz) plasma waves, although the presence of these waves has yet to be experimentally detected.^{18–20}

In this work, we have shown that low-frequency modes driven by the cathode electron azimuthal drift also are capable of heating and accelerating pole ions in the azimuthal direction, which increases the flux of ion kinetic energy to the pole region. These swirling ions, some of which will fall through the sheath potential toward the pole, will have not only their radial and axial velocities but the additional azimuthal velocity component contributing to their velocity and energy. This has the dual effects of increasing their impact kinetic energy and increasing their angle of incidence from normal. Both of these effects can increase the sputter yield for a particular ion,⁴⁹ preferentially sputtering in the azimuthal direction. For example, suppose that ions with

no azimuthal swirl impact the pole cover with incident kinetic energy totaling $E_i = 25$ eV after falling through the sheath, at an angle of incidence of $\alpha = 0^\circ$. This corresponds to an axial impact velocity of 6 km/s for singly charged xenon. Now, consider an ion with 8 km/s of azimuthal swirl velocity, corresponding to the tail of the velocity distributions measured in Fig. 5(a). Due to this azimuthal velocity, this ion will impact the pole with a significantly increased incident kinetic energy of $E_i \sim 68$ eV, in addition to gaining a pitch angle of $\alpha \sim 53^\circ$. Applying these factors to the evaluation of the Eckstein–Wei model fit for sputtering of graphite from single-charged xenon presented in Ref. 49, the contribution of this azimuthal swirl amounts to an increase in the sputter yield by a factor of approximately 280. This numerical example demonstrates the high sensitivity of pole sputtering rates to the 3D dynamics of the near-pole ion population, especially azimuthal drift effects.

Notably, while we do not have measurements of pole erosion for this study, we note that recent wear tests on the magnetically shielded AEPS Hall thrusters showed that when a masking material was placed on the cathode keeper, the erosion pattern demonstrated distinct azimuthal shadowing, suggesting that the ions impact the pole with significant azimuthal velocities. However, this effect was not observed on the inner front pole surface.²⁵ This is consistent qualitatively with the interpretation that for the surfaces closest to the cathode plume, the erosion is in part driven by azimuthal effects, leading to ions impacting the cathode keeper and poles at glancing angles pitched along the swirl direction. Our observations therefore strongly suggest that the anti-drift mode could be a contributing factor to the non-classical erosion rates at the cathode keeper and inner edge of the inner front pole of Hall thrusters with magnetic shielding. On a related note, if these wave effects remain present for operation with lighter gases such as krypton or argon, which generally have increased sputter yields for the same ion energy,⁵⁰ the implications for the erosion of the thruster could be further increased. If, as these results suggest, the anti-drift mode is a relevant source of ion acceleration and therefore contributes to inner front pole erosion, then suppressing the growth of this instability may enable the reduction of the pole erosion rate. Since the anti-drift mode grows at the expense of the electron diamagnetic drift energy and thus propagates azimuthally in the crossed-field plasma, it is possible that by modifying the field structure, electron-neutral collision frequency, or introducing physical barriers in the azimuthal direction, this azimuthal wave structure may be suppressed.

VII. CONCLUSION

In this work, we have experimentally characterized the ion dynamics across the inner front pole of a high-power, magnetically shielded Hall thruster with a centrally mounted cathode. To this end, we applied a time-averaged laser-induced fluorescence diagnostic to measure the distribution of azimuthal velocities for singly ionized xenon along the azimuthal direction. These measurements demonstrated ion swirl velocities exceeding 2.5 km/s in addition to ion temperatures greater than 8 eV at the interface between the cathode keeper and inner front pole cover, both of which cannot be explained by time-averaged, classical effects. We investigated this phenomenon further by applying a time-resolved LIF diagnostic, which showed that the ion properties are strongly coupled to a 90-kHz oscillation. This oscillation was previously identified as the anti-drift mode, a coherent, rotational wave which extracts energy from the gradient-driven electron drift.

Using this time-resolved data to supplement a 1D model of radial ion motion across the front pole cover of the thruster, we make the argument that these hot, swirling ions result from the action of the anti-drift mode. Our results suggest that these waves are capable of transferring this drift energy to the ion population via electrostatic heating and acceleration. Our model predictions agree with the observed time-averaged ion velocities and temperatures to within a factor of two, although due to physical simplifications and sparsity of wave amplitude data, the precise region of ion energization is located closer to the cathode centerline than predicted by this simulation, and results in much stronger acceleration than the model. These results demonstrate that the azimuthal anti-drift mode is an important mechanism for understanding the ion energies near the pole of Hall thrusters with central cathodes. Accounting for this effect will thus improve the accuracy of pole erosion models, and there is potential to increase thruster lifetimes if these waves can be mitigated.

ACKNOWLEDGMENTS

A portion of this research was carried out at the Jet Propulsion Laboratory (JPL), California Institute of Technology, under a contract with NASA (80 NM0018D0004). This work was supported by NASA Space Technology Graduate Research Opportunity (80NSSC20K1229). We wish to thank Leanne Su and Matthew Byrne for experimental assistance.

AUTHOR DECLARATIONS

Conflict of Interest

The authors have no conflicts to disclose.

Author Contributions

Parker John Roberts: Conceptualization (supporting); Data curation (lead); Formal analysis (lead); Investigation (lead); Methodology (equal); Resources (equal); Software (equal); Writing – original draft (lead); Writing – review & editing (lead). **Vernon H. Chaplin:** Conceptualization (supporting); Methodology (equal); Software (equal); Supervision (supporting); Writing – review & editing (supporting). **Benjamin A. Jorns:** Conceptualization (lead); Funding acquisition (lead); Methodology (equal); Project administration (lead); Supervision (lead); Writing – review & editing (supporting).

DATA AVAILABILITY

The normalized data that support the findings of this study are available from the corresponding author upon reasonable request.

REFERENCES

- J.-P. Boeuf, "Tutorial: Physics and modeling of Hall thrusters," *J. Appl. Phys.* **121**, 011101 (2017).
- D. M. Goebel and I. Katz, *Fundamentals of Electric Propulsion: Ion and Hall Thrusters* (John Wiley & Sons, 2008).
- D. Lev, R. M. Myers, K. M. Lemmer, J. Kolbeck, H. Koizumi, and K. Polzin, "The technological and commercial expansion of electric propulsion," *Acta Astronaut.* **159**, 213–227 (2019).
- I. G. Mikellides, I. Katz, R. R. Hofer, and D. M. Goebel, "Magnetic shielding of a laboratory Hall thruster. I. Theory and validation," *J. Appl. Phys.* **115**, 043303 (2014).
- R. R. Hofer, D. M. Goebel, I. G. Mikellides, and I. Katz, "Magnetic shielding of a laboratory Hall thruster. II. Experiments," *J. Appl. Phys.* **115**, 043304 (2014).
- J. D. Frieman, H. Kamhawi, P. Y. Peterson, D. A. Herman, J. H. Gilland, and R. R. Hofer, "Completion of the long duration wear test of the NASA HERMeS Hall thruster," AIAA Paper No. 2019-3895, 2019.
- R. R. Hofer, B. A. Jorns, J. E. Polk, I. G. Mikellides, and J. S. Snyder, "Wear test of a magnetically shielded Hall thruster at 3000 seconds specific impulse," in *33rd International Electric Propulsion Conference* (Electric Rocket Propulsion Society, 2013), pp. 1–24.
- R. W. Conversano, R. B. Lobbia, S. M. Arestie, A. Lopez-Ortega, V. H. Chaplin, S. W. Reilly, and D. M. Goebel, "Demonstration of one hundred kilogram xenon throughput by a low-power Hall thruster," *J. Propul. Power* **39**, 217–231 (2023).
- D. A. Herman, T. Gray, I. Johnson, T. Kerl, T. Lee, and T. Silva, "The application of advanced electric propulsion on the NASA power and propulsion element (PPE)," in *International Electric Propulsion Conference* (Electric Rocket Propulsion Society, 2019), No. GRC-E-DAA-TN72776.
- I. G. Mikellides, A. Lopez Ortega, and B. Jorns, "Assessment of pole erosion in a magnetically shielded Hall thruster," AIAA Paper No. 2014-3897, 2014.
- J. E. Polk, R. B. Lobbia, A. Barriault, P. Guerrero, I. G. Mikellides, and A. L. Ortega, "Inner front pole cover erosion in the 12.5 kW HERMeS Hall thruster over a range of operating conditions," in *35th International Electric Propulsion Conference* (Electric Rocket Propulsion Society, Atlanta, GA, 2017), No. IEPC-2017-409.
- I. G. Mikellides and I. Katz, "Numerical simulations of Hall-effect plasma accelerators on a magnetic-field-aligned mesh," *Phys. Rev. E* **86**, 046703 (2012).
- B. Jorns, C. A. Dodson, J. R. Anderson, D. M. Goebel, R. R. Hofer, M. J. Sekerak, A. Lopez Ortega, and I. G. Mikellides, "Mechanisms for pole piece erosion in a 6-kW magnetically-shielded Hall thruster," AIAA Paper No. 2016-4839, 2016.
- A. Lopez Ortega, I. G. Mikellides, M. J. Sekerak, and B. A. Jorns, "Plasma simulations in 2-D (r-z) geometry for the assessment of pole erosion in a magnetically shielded Hall thruster," *J. Appl. Phys.* **125**, 033302 (2019).
- S. E. Cusson, E. T. Dale, B. A. Jorns, and A. D. Gallimore, "Acceleration region dynamics in a magnetically shielded Hall thruster," *Phys. Plasmas* **26**, 023506 (2019).
- A. L. Ortega and I. G. Mikellides, "Investigations of pole erosion mechanisms in the 12.5 kW HERMeS Hall thruster with the Hall2De code," AIAA Paper No. 2018-4647, 2018.
- W. Huang and H. Kamhawi, "Counterstreaming ions at the inner pole of a magnetically shielded Hall thruster," *J. Appl. Phys.* **129**, 043305 (2021).
- A. Lopez Ortega, I. G. Mikellides, V. H. Chaplin, W. Huang, and J. D. Frieman, "Anomalous ion heating and pole erosion in the 12.5-kW Hall effect rocket with magnetic shielding (HERMeS)," AIAA Paper No. 2020-3620, 2020.
- I. G. Mikellides and A. Lopez Ortega, "Cross-field streaming instabilities in the lower hybrid frequency near the inner pole region of a Hall thruster," AIAA Paper No. 2020-3619, 2020.
- I. G. Mikellides and A. L. Ortega, "The dispersion of the modified two-stream and lower hybrid drift instabilities in the near-pole plume of a magnetically shielded Hall thruster," AIAA Paper No. 2021-3416, 2021.
- I. G. Mikellides and A. L. Ortega, "Growth of the modified two-stream instability in the plume of a magnetically shielded Hall thruster," *Phys. Plasmas* **27**, 100701 (2020).
- I. G. Mikellides and A. L. Ortega, "Growth of the lower hybrid drift instability in the plume of a magnetically shielded Hall thruster," *J. Appl. Phys.* **129**, 193301 (2021).
- B. A. Jorns and R. R. Hofer, "Plasma oscillations in a 6-kW magnetically shielded Hall thruster," *Phys. Plasmas* **21**, 053512 (2014).
- B. A. Jorns, S. E. Cusson, Z. Brown, and E. Dale, "Non-classical electron transport in the cathode plume of a Hall effect thruster," *Phys. Plasmas* **27**, 022311 (2020).
- J. D. Frieman, J. H. Gilland, H. Kamhawi, J. Mackey, G. J. Williams, Jr., R. R. Hofer, and P. Y. Peterson, "Wear trends of the 12.5 kW HERMeS Hall thruster," *J. Appl. Phys.* **130**, 143303 (2021).
- R. Davidson and N. Krall, "Anomalous transport in high-temperature plasmas with applications to solenoidal fusion systems," *Nucl. Fusion* **17**, 1313–1372 (1977).

- ²⁷A. Lopez Ortega and I. G. Mikellides, "The importance of the cathode plume and its interactions with the ion beam in numerical simulations of Hall thrusters," *Phys. Plasmas* **23**, 043515 (2016).
- ²⁸R. R. Hofer, S. E. Cusson, R. B. Lobbia, and A. D. Gallimore, "The H9 magnetically shielded Hall thruster," in *35th International Electric Propulsion Conference* (Electric Rocket Propulsion Society, 2017), pp. 2017–232.
- ²⁹E. A. Viges, B. A. Jorns, A. D. Gallimore, and J. Sheehan, "University of Michigan's upgraded large vacuum test facility," in *36th International Electric Propulsion Conference* (Electric Rocket Propulsion Society, 2019), pp. 1–18.
- ³⁰J. W. Dankanich, M. Walker, M. W. Swiatek, and J. T. Yim, "Recommended practice for pressure measurement and calculation of effective pumping speed in electric propulsion testing," *J. Propul. Power* **33**, 668–680 (2017).
- ³¹C. Durot, A. Gallimore, and T. Smith, "Validation and evaluation of a novel time-resolved laser-induced fluorescence technique," *Rev. Sci. Instrum.* **85**, 013508 (2014).
- ³²V. Chaplin, R. Lobbia, A. Lopez Ortega, I. Mikellides, R. Hofer, J. Polk, and A. Friss, "Time-resolved ion velocity measurements in a high-power Hall thruster using laser-induced fluorescence with transfer function averaging," *Appl. Phys. Lett.* **116**, 234107 (2020).
- ³³P. J. Roberts, V. H. Chaplin, A. Lopez Ortega, and I. G. Mikellides, "Impact of low-frequency oscillations on ion energy in a high-power magnetically shielded Hall thruster," *J. Appl. Phys.* **131**, 033301 (2022).
- ³⁴M. F. Konopliv, V. H. Chaplin, L. K. Johnson, and R. E. Wirz, "Accuracy of using metastable state measurements in laser-induced fluorescence diagnostics of xenon ion velocity in Hall thrusters," *Plasma Sources Sci. Technol.* **32**, 015009 (2023).
- ³⁵W. Huang, B. Drenkow, and A. Gallimore, "Laser-induced fluorescence of singly-charged xenon inside a 6-kW Hall thruster," AIAA Paper No. 2009-5355, 2009.
- ³⁶R. Cedolin, W. Hargus, Jr., P. Storm, R. Hanson, and M. Cappelli, "Laser-induced fluorescence study of a xenon Hall thruster," *Appl. Phys. B* **65**, 459–469 (1997).
- ³⁷V. H. Chaplin, R. W. Conversano, R. B. Lobbia, A. L. Ortega, I. G. Mikellides, R. R. Hofer, and B. A. Jorns, "Laser-induced fluorescence measurements of the acceleration zone in the 12.5 kW HERMeS Hall thruster," in *35th International Electric Propulsion Conference* (Electric Rocket Propulsion Society, 2017), Vol. 229, pp. 8–12.
- ³⁸P. J. Roberts, B. A. Jorns, and V. H. Chaplin, "Experimental characterization of wave-induced azimuthal ion velocities in a hollow cathode plume," AIAA Paper No. 2022-1561, 2022.
- ³⁹R. B. Lobbia and A. D. Gallimore, "Fusing spatially and temporally separated single-point turbulent plasma flow measurements into two-dimensional time-resolved visualizations," in *12th International Conference on Information Fusion* (IEEE, 2009), pp. 678–685.
- ⁴⁰D. M. Goebel, K. K. Jameson, R. M. Watkins, I. Katz, and I. G. Mikellides, "Hollow cathode theory and experiment. I. Plasma characterization using fast miniature scanning probes," *J. Appl. Phys.* **98**, 113302 (2005).
- ⁴¹J. Fife, M. Martinez-Sanchez, J. Szabo, J. Fife, M. Martinez-Sanchez, and J. Szabo, "A numerical study of low-frequency discharge oscillations in Hall thrusters," AIAA Paper No. 1997-3052, 1997.
- ⁴²V. H. Chaplin, J. E. Polk, I. G. Mikellides, A. L. Ortega, and P. J. Roberts, "Preparation for wave measurements using LIF, and comparison of ion velocities in cathode testing versus Hall thruster operation," in *37th International Electric Propulsion Conference* (Electric Rocket Propulsion Society, Massachusetts Institute of Technology, 2022), No. IEPC-2022-302.
- ⁴³M. Georgin, "Ionization instability of the hollow cathode plume," Ph.D. thesis (University of Michigan, 2020).
- ⁴⁴G. Becatti, D. M. Goebel, and M. Zuin, "Observation of rotating magnetohydrodynamic modes in the plume of a high-current hollow cathode," *J. Appl. Phys.* **129**, 033304 (2021).
- ⁴⁵G. Becatti, F. Buralassi, F. Paganucci, M. Zuin, and D. M. Goebel, "Resistive MHD modes in hollow cathodes external plasma," *Plasma Sources Sci. Technol.* **31**, 015016 (2022).
- ⁴⁶I. Kaganovich, Y. Raitses, D. Sydorenko, and A. Smolyakov, "Kinetic effects in a hall thruster discharge," *Phys. Plasmas* **14**, 057104 (2007).
- ⁴⁷I. Kaganovich, V. Demidov, S. Adams, and Y. Raitses, "Non-local collisionless and collisional electron transport in low-temperature plasma," *Plasma Phys. Controlled Fusion* **51**, 124003 (2009).
- ⁴⁸V. H. Chaplin, L. K. Johnson, R. B. Lobbia, M. F. Konopliv, T. Simka, and R. E. Wirz, "Insights from collisional-radiative models of neutral and singly ionized xenon in Hall thrusters," *J. Propul. Power* **38**, 866–879 (2022).
- ⁴⁹J. T. Yim, "A survey of xenon ion sputter yield data and fits relevant to electric propulsion spacecraft integration," in *International Electric Propulsion Conference (IEPC)* (Electric Rocket Propulsion Society, 2017), No. GRC-E-DAA-TN45154.
- ⁵⁰K. A. Zoerb, J. D. Williams, D. D. Williams, and A. P. Yalin, "Differential sputtering yields of refractory metals by xenon, krypton, and argon ion bombardment at normal and oblique incidences," in *29th International Electric Propulsion Conference* (Electric Rocket Propulsion Society, 2005), pp. 2005–293.